University of Reading

Current events at Saturn: ring–planet electromagnetic coupling

Article

Published Version

Creative Commons: Attribution 4.0 (CC-BY)

Open Access

Agiwal, O., Cao, H., Hsu, H.-W., Moore, L., Sulaiman, A. H., O'Donoghue, J. ORCID: https://orcid.org/0000-0002-4218-1191 and Dougherty, M. K. (2024) Current events at Saturn: ring–planet electromagnetic coupling. The Planetary Science Journal, 5 (6). 134. ISSN 2632-3338 doi: 10.3847/PSJ/ad4343 Available at https://centaur.reading.ac.uk/120070/

It is advisable to refer to the publisher's version if you intend to cite from the work. See Guidance on citing.

To link to this article DOI: http://dx.doi.org/10.3847/PSJ/ad4343

Publisher: IOP Publishing

All outputs in CentAUR are protected by Intellectual Property Rights law, including copyright law. Copyright and IPR is retained by the creators or other copyright holders. Terms and conditions for use of this material are defined in the End User Agreement.

www.reading.ac.uk/centaur

CentAUR

University of Reading

Central Archive at the University of Reading

Reading's research outputs online

The Planetary Science Journal, 5:134 (11pp), 2024 June https://doi.org/10.3847/PSJ/ad4343
© 2024. The Author(s). Published by the American Astronomical Society.
OPEN ACCESS

Current Events at Saturn: Ring–Planet Electromagnetic Coupling

Omakshi Agiwal[1], Hao Cao[2,3], Hsiang-Wen Hsu[4], Luke Moore[1], Ali H. Sulaiman[5], James O'Donoghue[6,7], and Michele K. Dougherty[8]
[1] Center for Space Physics, Boston University, MA, USA; oagiwal@bu.edu
[2] Department of Earth, Planetary, and Space Sciences, University of California, Los Angeles, CA, USA
[3] Department of Earth and Planetary Sciences, Harvard University, Cambridge, MA 02138, USA
[4] Laboratory for Atmospheric and Space Physics, University of Colorado, Boulder, CO, USA
[5] School of Physics and Astronomy, Minnesota Institute for Astrophysics, University of Minnesota, Minneapolis, MN, USA
[6] Department of Solar System Science, JAXA Institute of Space and Astronautical Science, Sagamihara 252-5210, Japan
[7] Department of Meteorology, University of Reading, Whiteknights Road, Reading, UK
[8] Blackett Laboratory, Imperial College London, London, UK
Received 2024 January 12; revised 2024 April 17; accepted 2024 April 17; published 2024 June 7

Abstract

This study presents a synthesized analysis of in situ and ground-based observations to investigate electromagnetic coupling between Saturn and its rings. During the Cassini Grand Finale, the magnetometer detected gradients in the azimuthal magnetic field B_ϕ connected to Saturn's B-ring on 17 out of 21 orbits. The B_ϕ gradients indicate that field-aligned currents are flowing into Saturn's B-ring at ∼1.55–1.67 R_S in the ring plane, preferentially in the southern hemisphere. On average, these currents are magnetically conjugate with ground-based observations of nonsolar enhancements in H_3^+ emissions from Saturn's ionosphere and detected contemporaneously with ring-sourced, planetward electron beams and field-aligned charged dust grain inflow from the C- and B-rings into Saturn's atmosphere. Collectively, these observations align with Voyager-era predictions of a phenomenon known as "ring rain," where charged ring material generated inward of a nominal "critical radius" is drawn into Saturn's upper atmosphere along the magnetic field. However, we show that the B-ring currents are not likely to be a direct signature of infalling field-aligned ring grains. Instead, we propose that the ring rain generation mechanism naturally results in a sharp gradient in the ionospheric Pedersen conductance at the ∼1.57–1.67 R_S boundary, which, combined with a $\boldsymbol{v} \times \boldsymbol{B}$ electric field in the ring ionosphere, could drive the observed B-ring currents. The Pedersen conductance in the high-conductance region of the southern ring ionosphere is constrained to ∼0.07–2 S and is observed to vary within this range on week-long timescales.

Unified Astronomy Thesaurus concepts: Planetary magnetospheres (997); Planetary rings (1254); Planetary ionospheres (2185); Saturn (1426)

1. Introduction

Saturn's magnetic field connects the low- and midlatitude planetary ionosphere to the D-, C-, B-, and A-rings in the equatorial/ring plane of Saturn's magnetosphere. The DCBA rings extend between ∼1.1 and 2.27 Saturn radii (R_S; where 1 R_S = 60,268 km is the equatorial radius of Saturn) in the equatorial plane and are listed in order of their proximity to the planet.

The Cassini spacecraft completed the final phase of its mission known as the "Grand Finale" in 2017 (Revs 271-292, where each Rev number is an orbit). During these orbits, Cassini repeatedly traversed the magnetic field lines that are connected to Saturn's rings near orbit periapsis. In this region, the Cassini magnetometer (MAG; Dougherty et al. 2004) measured strong spatial gradients in the azimuthal magnetic field component B_ϕ on magnetic field lines confined within the outer edge of Saturn's D-ring (Dougherty et al. 2018; Hunt et al. 2019; Provan et al. 2019c) and along the Enceladus flux tube (Sulaiman et al. 2018a), as well as weaker B_ϕ gradients on magnetic field lines connected to Saturn's B-ring (Provan et al. 2019c; Sulaiman et al. 2019; Agiwal et al. 2021). Due to the highly axisymmetric nature of Saturn's internal magnetic field around the spin axis (Dougherty et al. 2018; Cao et al. 2020), spatial gradients in measured B_ϕ are likely supported by field-aligned currents. This study aims to investigate the driver of the B-ring field-aligned currents.

Empirical models suggest that the intra D-ring currents are driven by interhemispheric wind shears in Saturn's upper atmosphere (Khurana et al. 2018; Provan et al. 2019c; Agiwal et al. 2021) that are analogous to a wind-shear driven current system also observed at Earth (Buchert 2020). However, Agiwal et al. (2021) showed that the sense of the angular velocity shear from empirically constrained thermospheric zonal winds at Saturn (Brown et al. 2020) predicts a southward field-aligned current in the magnetosphere on B-ring flux tubes, whereas Sulaiman et al. (2019) and Agiwal et al. (2021) showed that the observed B_ϕ gradients are consistent with a northward field-aligned current in the southern magnetosphere. Thus, Agiwal et al. (2021) speculated that the intra D-ring and B-ring current systems may be driven by different mechanisms.

Sulaiman et al. (2018b, 2019) reported Cassini Radio and Plasma Waves Science (RPWS; Gurnett et al. 2004) measurements of field-aligned electron beams flowing from the rings into Saturn's upper atmosphere in both hemispheres, which is consistent with the northward B-ring currents detected in the southern magnetosphere. However, the proposed generation mechanism for the RPWS measurements assumes field-aligned electron beams originating at ∼1.85 R_S in the ring plane (further described in Section 2), whereas the ring plane

Original content from this work may be used under the terms of the Creative Commons Attribution 4.0 licence. Any further distribution of this work must maintain attribution to the author(s) and the title of the work, journal citation and DOI.

magnetic mapping of the B-ring currents lies $\geqslant 0.2\,R_S$ radially inward of this boundary. Therefore, the connection between these two data sets requires further investigation.

In this study, we present a synthesized analysis of the B_ϕ gradients connected to the B-ring with other observations and models to consolidate our understanding of electromagnetic interactions between Saturn and its rings. We introduce the theory and observations relevant to our investigation in Section 2. Discussion of the trends in the B_ϕ measurements and comparison with other data sets and models are presented in Section 3. Conclusions and outstanding questions are presented in Section 4.

2. Electromagnetic Ring–Planet Coupling at Saturn: Theory and Observations

Northrop & Hill (1982) proposed electromagnetic coupling between the rings and the midlatitude ionosphere in the form of a field-aligned "siphon flow" of charged material from the rings into the planet (also known as "ring rain") inside of a nominal boundary in the ring plane, which is defined as the "critical radius" r_C.

Submicrometer-sized icy grains in Saturn's rings can gain charge through photoionization or micrometeorite impact ionization (Connerney 2013), after which the motion of grains with a sufficiently high charge-to-mass ratio ($q/m \rightarrow 10^3\,\mathrm{C\,kg^{-1}}$) is governed by gravitational, centrifugal, and magnetic mirror forces. Northrop & Hill (1982) show that inside r_C, gravity dominates the centrifugal force when evaluated along the field line B, which results in ring grains being lost to Saturn's atmosphere along the magnetic field, i.e., *ring rain*. Outside r_C, the centrifugal force dominates when evaluated along the magnetic field B; thus, charged ring grains remain confined to the ring plane. Consequently, Northrop & Hill (1983a) and Ip (1983) anticipated magnetically conjugate discontinuities in the ring plane and Saturn's atmosphere associated with the critical radius.

The location of the critical radius depends on the thermal energy and magnetic moment of high q/m charged material (Northrop & Hill 1982, 1983a; Ip 1984; Connerney 1986). For example, the r_C for charged grains with thermal energy $\leqslant 2$ eV and zero magnetic moment is evaluated at $\sim 1.62\,R_S$. Meanwhile, freshly ionized pickup ions that were initially in Keplerian orbit around Saturn have a nonzero magnetic moment and thus also feel the magnetic mirror force. This has the net effect of moving r_C radially inward to $\sim 1.525\,R_S$, and only ions inside this boundary are lost to Saturn's atmosphere. Sharp boundaries in ring optical depth exist at both $\sim 1.53\,R_S$ and $\sim 1.62\,R_S$, marking the inner edge of the B-ring and the boundary between the "inner" and "outer" B-ring, respectively (Northrop & Hill 1983a).

Furthermore, nonsolar variations have been observed in the reflected light from Saturn's atmosphere (Connerney 1986) and ionospheric H_3^+ emissions (O'Donoghue et al. 2013, 2017, 2019) at latitudes that are magnetically connected to $\sim 1.53\,R_S$ and $\sim 1.62\,R_S$ in the ring plane. H_3^+ is the dominant molecular ion in Saturn's upper atmosphere, and the nonsolar latitudinal trends in the densities derived from the ion emissions were shown to be consistent with model predictions of charged water influx into Saturn's midlatitude ionosphere (Moore et al. 2015). Finally, the Cassini Cosmic Dust Analyzer (CDA; Srama et al. 2004) measured a large influx of dusty rain grains equatorially inflowing from Saturn's rings into the planetary atmosphere during the Cassini Grand Finale (Hsu et al. 2018). The flux extends to higher latitudes further away from the equator and is magnetically connected to the C- and B-rings. These observations serve as strong indirect evidence for electromagnetic coupling between Saturn and its rings, where the presence of the magnetic field is eroding the rings and altering the atmospheric chemistry.

Another theory proposing how Saturn's rings and the planet interact electromagnetically was presented by Xin et al. (2006). The ions in Saturn's equatorial magnetosphere are expected to corotate with the planetary magnetic field, however the neutral ring particles orbit with Keplerian velocities. The Kronosynchronous orbital boundary (KSO) defines the location where the ions and Keplerian neutrals would be synchronous in the ring plane and is theoretically located at $\sim 1.85\,R_S$. Inside the KSO boundary, neutral ring particles are super-corotational in the ion rest frame, while outside, they are subcorotational. Xin et al. (2006) show that the difference in the ion-neutral ring particle angular velocity would result in a diverging $\boldsymbol{v} \times \boldsymbol{B}$ electric field and, therefore, a diverging radial current at the KSO boundary that would close within Saturn's magnetosphere and ionosphere as a field-aligned current.

Xin et al. (2006) used this theory to explain Cassini RPWS observations of plasma waves traveling in the whistler mode, known as "auroral hiss," along magnetic field lines connected to the B-ring during Saturn Orbital Insertion in 2004. These observed waves are created by a beam-plasma instability, providing indirect evidence of electron beams. The distribution of these electron beams, inferred from the auroral hiss pattern, aligns with the flow of currents into the ring plane. According to Xin et al. (2006), the source of these electron beams is estimated to be located near $\sim 1.76\,R_S$ (hereafter the X06 boundary); however, the authors were unable to explain why the observed electron beam source would be located radially inward of the theoretical KSO boundary.

Assuming the existence of a ring ionosphere (a layer of ionized material directly above and below the rings in the ring plane) with a finite effective Pedersen conductance, which has been predicted by various models (Bouhram et al. 2006; Johnson et al. 2006; Luhmann et al. 2006; Tseng et al. 2010, 2013), the generation of the proposed current system is a natural outcome of the ion-neutral velocity shear in the ring plane. Therefore, Sulaiman et al. (2019) suggested that the Cassini Grand Finale RPWS detection of planetward field-aligned electron beams originating in the rings was likely generated by the Xin et al. (2006) field-aligned current system (hereafter referred to as the Xin current system).

Sulaiman et al. (2019) are unable to map an electron beam emission source directly to Saturn's rings due to large bite-outs in the upper-frequency cutoff of the whistler mode wave emissions. However, Farrell et al. (2018) show that these bite-outs are indicative of electron density cavities on magnetic field lines that map to ~ 1.5–$2.3\,R_S$ in the ring plane. Typically, such measurements of density cavities strongly favor large field-parallel electric fields that are consistent with the presence of field-aligned currents. However, the interpretation of these results is complicated by the electron density cavity being observed in a region of the magnetosphere that is in the ring shadow (Hadid et al. 2018).

A summary of the observations and theoretical concepts considered in this study is presented in Figure 1. A meridional view of the near-Saturn space environment including Saturn, the rings, and Saturn's northward-offset internal magnetic field is

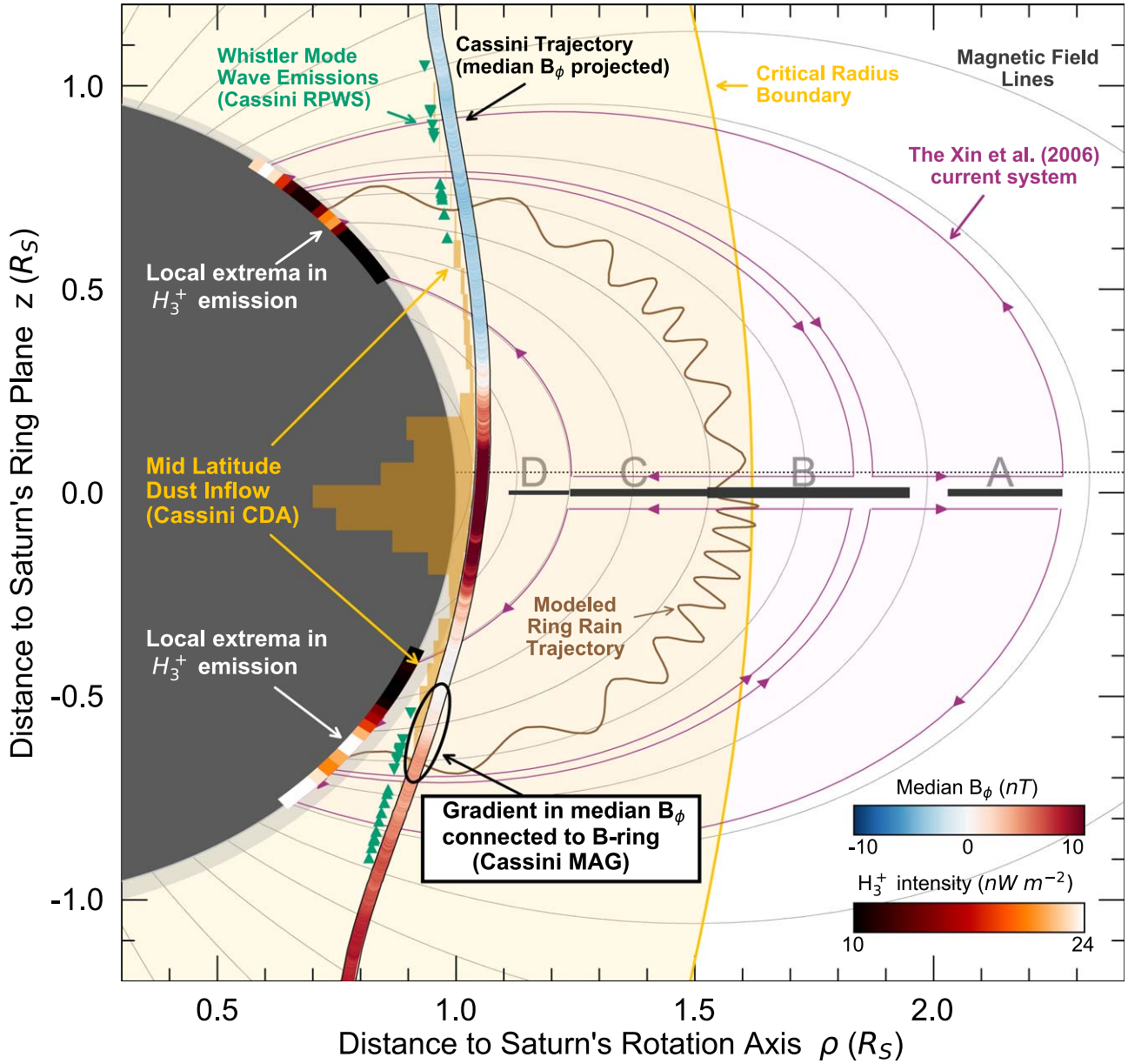

Figure 1. A meridional view of Saturn is shown in cylindrical (ρ, z) coordinates. The planetary magnetic field is shown using gray contours, and the planetary rings are shown by gray slabs at $z = 0$ R_S. Solid black lines indicate a representative spacecraft trajectory near orbit periapsis from the Cassini Grand Finale. Projected along the trajectory are in situ Cassini measurements of the median B_ϕ from MAG (blue–red color bar), dust impact rates from CDA (yellow histogram), and whistler mode wave emissions from RPWS (downward and upward green triangles indicate the start and stop locations of individual whistler mode emission intervals) from the Grand Finale. The current system proposed by Xin et al. (2006) is indicated by the shaded pink region. The direction of current flow is indicated by pink solid lines and arrows. The ring plane position of the Kronosynchronous orbital boundary (KSO) at $\rho \sim 1.85$ R_S and the RPWS whistler mode wave emission source constrained by Xin et al. (2006) are indicated. The "critical radius" r_C boundary is shown by a solid yellow line, which scales with latitude λ as $r^3 = r_C^3 \mathrm{cosec}^2(\lambda)$. The shaded yellow region within is where models predict ionospheric siphoning of ring plasma, or "ring rain." Modeled trajectories of charged dust grains flowing from the rings to the ionosphere along B are shown in brown. Finally, H_3^+ ion emissions (white–red–black color bar) from remote observations of Saturn's upper atmosphere in ~2011 are projected at their observed latitudes on Saturn's surface.

presented in cylindrical (ρ, z) coordinates, where $\rho = \sqrt{x^2 + y^2}$ is the perpendicular distance from Saturn's spin/dipole axis and z is aligned with Saturn's spin/dipole axis and positive northward.

The smoothed profile of the median azimuthal magnetic field B_ϕ observations from 21 Grand Finale orbits (Rev 277 is excluded due to missing data) is projected along a representative Cassini trajectory from the Grand Finale orbits, where the negative and positive B_ϕ measurements are shown using a blue–red color bar in Figure 1. Physically, a negative B_ϕ represents a lagging magnetic field and a positive B_ϕ represents a leading magnetic field in the northern hemisphere, and the opposite is true for the southern hemisphere. The sharp gradient in median B_ϕ in the intra D-ring region shows the wind-driven interhemispheric intra D-ring currents discovered during the Grand Finale (Dougherty et al. 2018). Strong gradients in median B_ϕ connected to the B-ring are seen in the southern hemisphere and circled in Figure 1, which is the focus of this study. A conjugate gradient in median B_ϕ is not observed in the northern hemisphere.

A yellow histogram presenting the average in situ CDA dust impact rate registered on the Chemical Analyzer Target (CAT)

from eight Grand Finale orbits (Hsu et al. 2018) is projected along the spacecraft trajectory in Figure 1. The H_3^+ ion emissions from remote observations of Saturn's ionosphere taken in 2011 (O'Donoghue et al. 2013) are projected on the edge of Saturn's surface in Figure 1 using a black–red–white color scale. Although there are more recent reports of nonsolar latitudinal variations in H_3^+ emissions at Saturn (O'Donoghue et al. 2017, 2019) that show the same overall latitudinal trend, the O'Donoghue et al. (2013) emissions have the highest spatial resolution and show magnetically conjugate emissions in both hemispheres. The nominal critical radius boundary at $\sim$1.62 R_S is shown using a solid yellow line in Figure 1. Modeled trajectories of charged dust grains originating in the ring plane are shown by solid brown lines in the northern and southern hemispheres (Hsu et al. 2018).

The Xin current system is shown in Figure 1 by the pink shaded region. The corresponding intervals of RPWS whistler mode wave emissions are indicated using green triangles along the spacecraft trajectory, where their up and down orientation indicates the start and end of the intervals, respectively. The theoretical KSO boundary located at $\sim$1.85 R_S and the X06 plasma wave emission source located at $\sim$1.76 R_S (Xin et al. 2006) are also indicated in Figure 1.

2.1. Cassini MAG Data from the Grand Finale Orbits

In addition to the median B_ϕ presented in Figure 1, we show the in situ azimuthal magnetic field B_ϕ observations from 21 Grand Finale orbits (Revs 271-292, except Rev 277 due to missing data) organized by L-shell from the inbound and outbound segments of the orbits in Figures 2(a) and (b), respectively. The L-shell corresponds to a given magnetic field line that intersects the equatorial plane at a radial distance $\rho = L$. Individual orbits are not identified in Figures 2(a) and (b), since the intent of the figure is simply to highlight statistical trends in the raw data, which are captured by the median B_ϕ profile presented in Figures 2(a) and (b). The median B_ϕ profile is calculated by binning the data across all orbits into 1° colatitude bins $\Delta\theta_i$ and then calculating the median. Here, θ_i is the magnetically mapped colatitude of the local ionospheric footpoint of the in situ measurements.

The B-ring signature can be identified in Figure 2(b), where the median B_ϕ measured in the southern hemisphere on the outbound segment of the Grand Finale orbits presents clear gradients on L-shells connected to both the C- and B-ring. Meanwhile, no significant gradients are observed in the median B_ϕ presented in Figure 2(a) for data taken along the inbound segment of the orbits in the northern hemisphere.

The B_ϕ amplitude over the rings is variable from orbit to orbit. This amplitude variability is thought to be associated with an ionospheric perturbation source known as planetary period oscillations (PPOs; see Carbary & Mitchell 2013, and references therein) that drives large-scale, interhemispheric field-aligned currents that close in Saturn's middle magnetosphere (e.g., Andrews et al. 2008; Hunt et al. 2014). PPOs are observed as a $\sim$10.6 hr sinusoidal modulation in magnetic field measurements. The measurements presented in Figures 2(a) and (b) span a total of $\sim$20 minutes UT and $\sim$1 hr in local time for each segment. As explained by Provan et al. (2019a), the effect of PPOs on such timescales would simply be to introduce an overall constant, nonzero contribution to B_ϕ. Therefore, the gradients in B_ϕ connected to the B- and C-rings in Figure 2(b) are signals of additional, local field-aligned currents.

We derive field-aligned current densities $j_{||}$ from the magnetic field measurements by using the detailed method outlined in Appendix A of Hunt et al. (2019). Note that the magnitude of $j_{||}$ is insensitive to the absolute value of B_ϕ and sensitive only to gradients in B_ϕ. Therefore, there is no need to try and subtract the background PPO perturbation field from the data at this stage. In summary:

1. We use Ampére's law to first derive the ionospheric meridional current per azimuth radian $I_m(\theta_i)$ flowing in Saturn's ionosphere from the B_ϕ measurements for the inbound and outbound segments of each orbit using Equation (1):

$$B_\phi(\theta_i) = \frac{\mu_0 I_m(\theta_i)}{\rho_{sc}}. \quad (1)$$

   Here, μ_0 is the magnetic constant, and ρ_{sc} is the perpendicular distance between Saturn's dipole axis and the spacecraft.
2. The meridional current $I_m(\theta_i)$ is binned into $\sim$1° colatitude bins and averaged. While binning the $I_m(\theta_i)$ for each orbit eliminates the digitization noise of the MAG data, a standard deviation σ on the binned data is computed and propagated forward.
3. Gradients in adjacent colatitude bins of $I_m(\Delta\theta_i)$ are computed along an ionospheric element of length ds on an oblate Saturn from Equations (A4) and (A5) from Hunt et al. (2019).
4. The spatial gradients in I_m are evaluated along the magnetic field B to derive the field-aligned current density $j_{||}$ at the spacecraft position using Equations (A6)–(A8) from Hunt et al. (2019).

The field-aligned current densities that satisfy the condition $(j_{||} \pm 1.5\sigma) \neq 0$ nA m^{-2} are presented as a function of the L-shell for each orbit in Figures 2(c) (inbound segments) and (d) (outbound segments). The 1.5σ uncertainty typically ranges between $\sim$60% and 99% of the derived $j_{||}$ value and ensures that only very conservative estimates of $j_{||}$ are presented in Figure 2. In this study, $j_{||}$ is defined as positive when aligned with the direction of Saturn's background magnetic field, which is oriented southward in the magnetosphere.

Box-and-whisker diagrams in Figures 2(c) and (d) indicate the median (solid horizontal line), interquartile range (box), and interdecile range (whiskers) for the $j_{||}$ L-shell distribution in both hemispheres. However, the very limited sample size of field-aligned current observations in the northern hemisphere means that constraining any "typical" behavior in this region is not statistically meaningful and therefore will not be utilized much in our discussion. The distributions shown in Figure 2 also exclude the data points from L-shells $<$1.24 R_S, since they are a signature of the intra D-ring current, and our discussion will focus primarily on the main ring-connected field-aligned currents.

Figures 2(c) and (d) also include the CDA impact rate for Revs 278, 280, 287, and 291, where the CDA detector had favorable pointing during the outbound leg of each orbit (Hsu et al. 2018). The observational geometry of the CDA detector was highly variable from orbit to orbit during the Grand Finale; therefore, orbits with unfavorable pointing are not shown. Impact rates greater than $>$0.1 s^{-1} are measured on C- and B-ring connected L-shells during the outbound segments of each of the orbits where the CDA CAT detector had favorable pointing. However, the same is not true for the northern hemisphere; e.g., Rev 278.

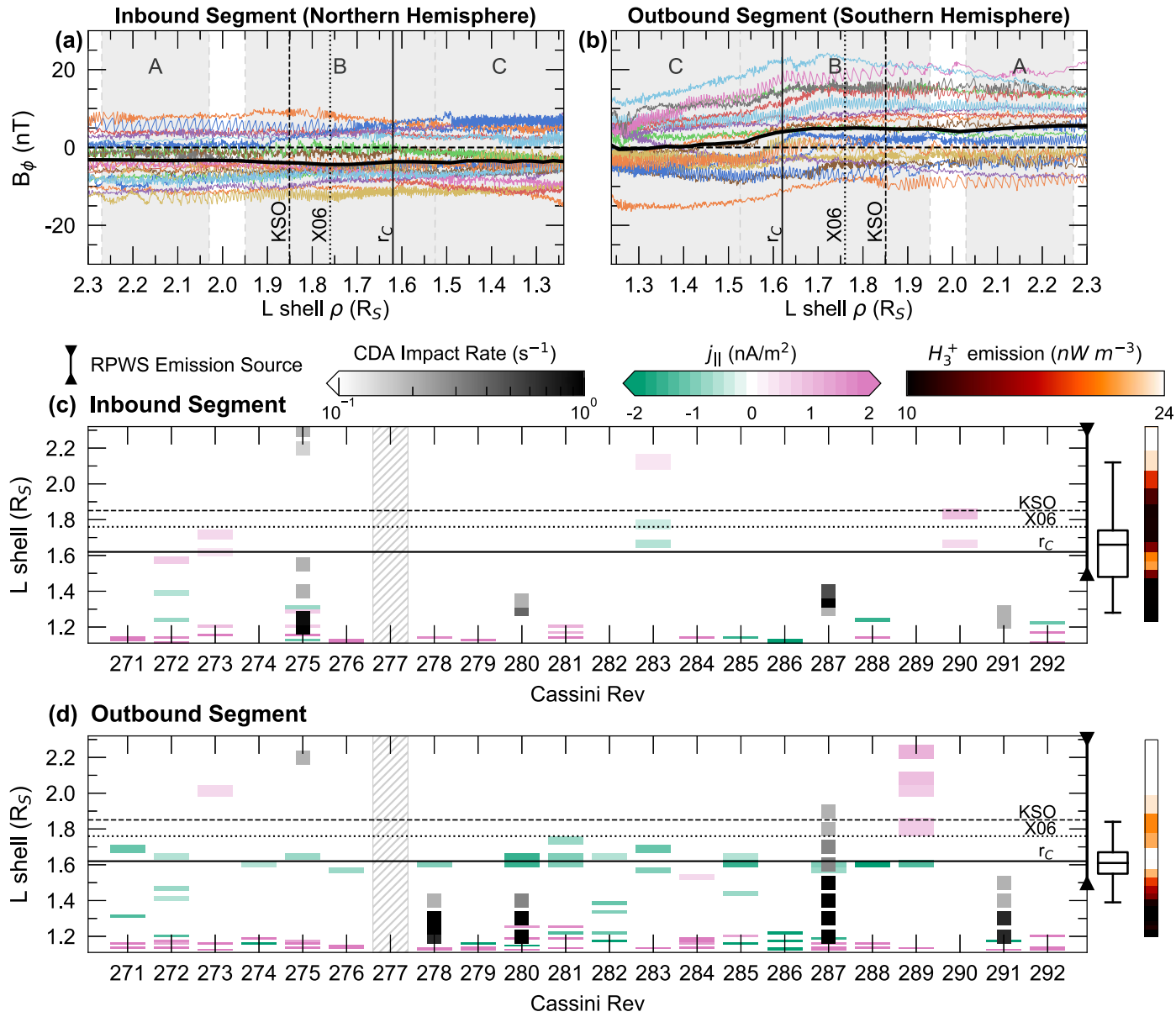

Figure 2. In situ B_ϕ measurements taken by Cassini MAG on ring-connected magnetic field lines are shown for 21 out of 22 Grand Finale orbits (Revs 271-292) in panels (a) and (b). Rev 277 is omitted due to missing data in the region of interest. The data are shown at 1 s resolution and organized by magnetic L-shell. The data from individual orbits are shown by different colored solid lines, and the median B_ϕ from the (a) inbound ($z > 0$ R_S) and (b) outbound ($z < 0$ R_S) segments of all the orbits is shown by a thick solid black line. The L-shell mapping of Saturn's rings is indicated by shaded gray regions. Panels (c) and (d) show the field-aligned currents $j_{||}$ derived from the gradients in B_ϕ for the (c) inbound and (d) outbound segment of each orbit as a function of the L-shell. The $j_{||}$ are positive (pink) when flowing in the same direction as the background magnetic field. Black dashed, dotted, and solid lines indicate the Kronosynchronous Orbit (KSO $\sim$ 1.85 R_S; dashed), the X06 emission source ($\sim$1.76 R_S), and the cold plasma critical radius ($r_C \sim 1.62$ R_S; solid) on all panels. Black box-and-whisker plots outside the main axes in panels (c) and (d) show the median (solid horizontal line), interquartile range (box), and interdecile range (whiskers) of the L-shell mapping of the $j_{||}$ signatures. The L-shell mapping of the CDA CAT impact rates, the H_3^+ emissions, and the RPWS constraints on the whistler wave emission source are also indicated on panels (c) and (d). The B_ϕ measurements and $j_{||}$ distributions presented in this figure can be found on Zenodo: doi:10.5281/zenodo.10823289 (Agiwal 2024).

Finally, the L-shell mapping of the H_3^+ emissions and the RPWS-derived constraints on the whistler mode wave emission source from Xin et al. (2006) and Sulaiman et al. (2019) are also presented in Figures 2(c) and (d) for easier comparison with the other data sets.

3. Discussions

3.1. North–South Asymmetries in the Observations

The field-aligned currents observed during the inbound and outbound segments of the Grand Finale orbits show significant hemispheric asymmetries in occurrence, L-shell mapping, and magnitude.

Figure 2(c) shows that field-aligned currents are observed on the inbound segment of 4 out of 21 Grand Finale orbits, whereas they are observed on the outbound segment of 16 Grand Finale orbits. The average $|j_{||}|$ observed on the inbound segments has a magnitude of $\sim 0.5 \pm 0.3$ nA m^{-2}, where the error stated is the 1σ uncertainty. The typically positive $j_{||}$ indicates that field-aligned currents flow from Saturn into the ring plane in the northern hemisphere. In contrast, the average $j_{||}$ observed in the southern hemisphere is $\sim -0.8 \pm 0.4$ nA m^{-2}, which agrees with the median northern hemisphere $j_{||}$ amplitude within the error but

indicates that the southern hemisphere field-aligned currents are also flowing into Saturn's ring plane.

Although there is some orbit-by-orbit variability in the L-shell mapping of the field-aligned currents, the interquartile range of the $j_{||}$ L-shell distribution is well constrained to $\sim$1.55–1.67 R_S on the outbound segments. Meanwhile, on the limited orbits where field-aligned currents were observed during the inbound segments, the $j_{||}$ L-shell distribution appears to be much broader.

In contrast, the field-aligned currents derived from the intra D-ring magnetic field signature showed strong hemispheric symmetry between conjugate magnetic latitudes (Hunt et al. 2019; Provan et al. 2019b), which can be seen even from a cursory glance from the $j_{||}$ distribution at L-shell $<$1.23 R_S in Figures 2(c) and (d). The symmetry implies current continuity between the northern and southern hemispheres, thus indicating interhemispheric electromagnetic coupling within the planetary atmosphere. The absence of hemispheric symmetry with the B-ring signature therefore indicates that it is unlikely to be generated by the same interhemispheric mechanism that drives the intra D-ring currents, as speculated by Agiwal et al. (2021).

There is a $\sim$3 hr local time difference between the inbound and outbound crossing of the B-ring flux tube, where the inbound crossing occurs in the pre-noon local time sector and the outbound crossing in the post-noon sector. However, Saturn's midlatitude ionospheric conditions are not expected to vary significantly over the local times sampled by Cassini (Müller-Wodarg et al. 2019; Agiwal et al. 2021); therefore, an interhemispheric current system that may vary in local time also seems unlikely. Thus, we conclude that the B-ring field-aligned current must be generated by electromagnetic coupling between the planetary ionosphere and an external magnetospheric plasma source, which can only be Saturn's rings within an L-shell of $\sim$2.3 R_S. Such distances are well inside of Enceladus's orbit, which is the primary source of magnetospheric plasma outside of $\sim$3 R_S (Persoon et al. 2020).

Hemispheric asymmetries are also evident in the CDA nanograin dust influx and H_3^+ emissions, with a stronger signal in the southern hemisphere (see Figure 1). In fact, O'Donoghue et al. (2019) report an "overflow" region of unusually high water influx (Moore et al. 2015) between $\sim$25° and 35° latitude in the southern hemisphere, which magnetically connects to the C-ring and is consistent with latitudes where the CDA reported charged nanograin influx. The RPWS instrument detected whistler mode wave emissions on the inbound segments of nine Grand Finale orbits and the outbound leg of 11 orbits (see Figure 1). While this is not as strong an asymmetry as that observed in the other data sets, there is still a trend of preferential detection in the southern hemisphere that suggests either that all aforementioned observations may share a common generation source or that the two generation mechanisms outlined in Section 2 produce complementary trends in the magnetosphere and ionosphere.

The hemispheric asymmetry between the various data sets can also be used to infer charged dust grain properties near the ring plane. Ip et al. (2016) present simulated trajectories of both negative and positively charged dust grains with high q/m ratios when launched from Saturn's ring plane with variable velocities. They find that irrespective of launch velocity, negatively charged dust grains launched inside the critical radius preferentially always flow into the southern hemisphere. Meanwhile, the deposition hemisphere of the positively charged dust grains depends on the initial launch direction from the rings. However, nanometer-sized grains carry only a small amount of electric charge, meaning that the amount of charge carried on ring rain grains may fluctuate stochastically once the grains are lofted from the rings, such that the charge polarity may even flip (Hsu et al. 2018). Since the lofting direction of ring rain is not expected to be selective, the stronger CDA and H_3^+ emission signals in the southern hemisphere likely suggest that the near-ring plasma environment preferably leads to negative grain potential, which is consistent with previous modeling assumptions (Hsu et al. 2018) based on in situ Langmuir probe results (Wahlund et al. 2018).

3.2. Investigating a Common Generation Source for All Observations

Various models of ring plasma dynamics (e.g., Luhmann et al. 2006; Tseng et al. 2010, 2013; Ip et al. 2016; Hsu et al. 2018) predict a hemispheric asymmetry in charged ring grain precipitation at Saturn due to the northward offset of Saturn's dipole magnetic equator relative to the ring plane. The models show that the planetward component of the magnetic field in the ring plane results in a preferentially southward flow of charged ring material inside the critical radius irrespective of Saturnian season, and only charged grains with extremely high velocities are able to escape northward. Thus, a stronger signal in the southern hemisphere is consistent with the ring rain generation mechanism, although the weaker northern hemisphere signature is only consistent with the ring rain mechanism if a high-velocity charged ion/grain population can be generated in the vicinity of the ring plane, for example, by meteroid impact ionization (Ip 1984).

Models of the ring atmosphere presented by Tseng et al. (2010) show that the ring ionosphere is a spatially and temporally variable structure, where the dominant O^+ ion densities are highly asymmetric above and below the ring plane within $\sim$1.7 R_S. Tseng et al. (2010) find that the ion densities are larger below the ring plane irrespective of Saturnian season, although the peak ion densities are typically larger at solstice and smaller at equinox. Typically, the Pedersen conductance scales linearly with ion density (although the presence of charged dust can alter this relationship), and a larger Pedersen conductance in the southern hemisphere would also facilitate a stronger ionospheric current (e.g., Agiwal et al. 2021) in the ring plane for the current system proposed by Xin et al. (2006). Therefore, the north–south asymmetry could be consistent with both the ring rain and the Xin current system generation mechanisms.

Figure 2 shows that the L-shell mapping of the B-ring field-aligned currents is variable from orbit to orbit, with typical ranges of $\sim$1.55–1.67 R_S in the southern hemisphere and $\sim$1.48–1.74 R_S in the northern hemisphere. Figure 2 also shows that the CDA nanograin dust impact rates typically peak at $\sim$1 impact per second on magnetic field lines that lie inward of the $\sim$1.4 R_S L-shell and then decrease in amplitude with increasing L-shell out to $\sim$1.5 R_S on Revs 278, 280, and 291 and $\sim$1.9 R_S on Rev 287 in the southern hemisphere. The peak H_3^+ ion emissions shown in Figures 1 and 2 are magnetically connected to the ring plane at $\sim$1.55–1.65 R_S in the southern hemisphere and $\sim$1.5–1.6 R_S in the northern hemisphere. Finally, the RPWS observations from the Cassini Grand Finale indicate that a whistler mode wave emission source lies between $\sim$1.5 and

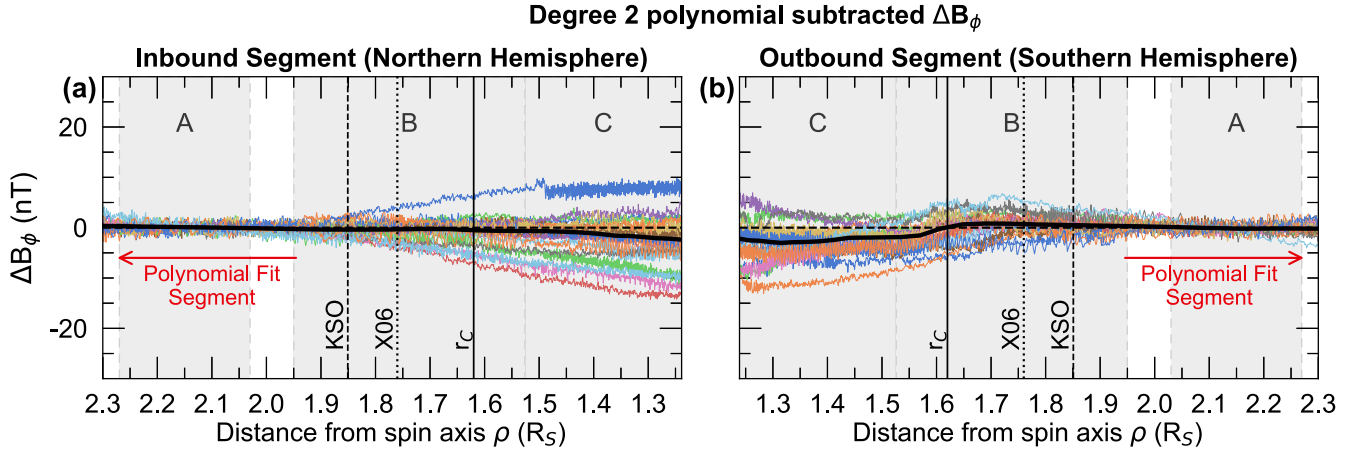

Figure 3. This figure has the same format as Figures 2(a) and (b), except it shows $n = 2$ polynomial subtracted ΔB_ϕ measurements that serve as a proxy for removing the effects of the PPO and auroral field-aligned current perturbation fields. The red arrows indicate the region mapping to the L-shell between ∼1.95 and 2.6 R_S (B-ring outer edge to A-ring inner edge, respectively). The $n = 2$ polynomial was fit only to the data in this region and then subtracted from the MAG data connected to the A–C rings.

2.3 R_S in the ring plane, as shown in Figures 1 and 2, where Xin et al. (2006) constrained an emission source to ∼1.76 R_S in the ring plane.

The location of the nominal critical radius depends on the ring plasma parameters, as discussed earlier. According to Northrop & Hill (1982), the critical boundary shifts inward from approximately 1.62 R_S for ions with lower q/m ratios. Additionally, Ip (1984) showed that the critical radius of O^+ ions generated by impact ionization can be defined by a range of L-shell values that depends on the energy and pitch angle of the ions. Higher-energy O^+ ions have a wider critical radius range, within which ions with smaller pitch angles are more likely to be lost to Saturn's atmosphere.

Ip (1984) estimated the critical radius L-shell range for ∼0.3 eV O^+ ions to be ∼1.6–1.7 R_S and ∼3 eV O^+ ions to be ∼1.5–2 R_S. This range is coincident with both the typical L-shell distribution of field-aligned currents and the local extrema in H_3^+ emissions in the southern hemisphere. Although there is also some overlap between the northern hemisphere H_3^+ emission signal and $j_{||}$ L-shell distribution, we reiterate that there are too few field-aligned current detections in the northern hemisphere to meaningfully constrain any "typical" behavior for detailed comparison with other data sets. Therefore, we will focus the remainder of this discussion primarily on trends in the southern hemisphere.

The magnetic conjugacy between the L-shell mapping of $j_{||}$ and the extrema in H_3^+ emissions suggests that a common generation source may be plausible. However, Figure 2(d) shows that the CDA detector consistently recorded ⩾1 impact per second on L-shells within ∼1.6 R_S during the outbound leg of Rev 287. At the same time, field-aligned currents were only observed close to the ∼1.6 R_S L-shell. This result is unsurprising, seeing as any currents generated by the much heavier and slower icy nanograins would be much harder to detect in an environment with other, stronger sources (i.e., electrons). However, it does suggest that field-aligned precipitation of charged dust grains and field-aligned currents must be different manifestations of the same process, if they are in fact generated by the same source mechanism.

The anticipated indicators of the ring rain generation mechanism included the H_3^+ emissions and CDA charged dust grain detections. Correspondingly, the field-aligned currents flowing into Saturn's rings and the planetward electron beams inferred from RPWS observations were the expected manifestations of the Xin current system.

The differential form of Ampère's law can be used to show that the B_ϕ associated with the Xin current system should result in positive spatial B_ϕ gradients along the spacecraft trajectory on both the inbound and outbound segments of the Cassini Grand Finale orbits. Since the generation process requires a diverging electric field where the velocity shear between the ions and neutrals should go to zero, the B_ϕ signature along the spacecraft trajectory should also change sign from negative to positive, with $B_\phi = 0$ nT at the KSO boundary in the absence of any external current systems.

Figures 1 and 2(b) show that a positive gradient in B_ϕ is repeatedly observed on the outbound leg of most of the Grand Finale orbits and is thus consistent with the Xin generation mechanism. However, the measurements presented in Figure 2 cannot be used to directly compare spatial trends in the observed B_ϕ with the expected trends from the Xin current system due to the nonzero contribution of external perturbation fields, such as PPOs and the auroral field-aligned currents, to the data set.

The PPO perturbation field is expected to be a ∼4.5 hr perturbation for the data interval presented in Figure 2, where PPOs typically manifest as a sinusoidal perturbation with a ∼10 hr period. Thus, we subtract an $n = 2$ polynomial, which is consistent with the profile of approximately half of a sine wave, from the I_m profiles for each orbit as a proxy for PPO subtraction. The utilization of a degree 2 polynomial likely eliminates large-scale perturbations caused by auroral field-aligned currents as well. Details regarding the polynomial subtraction are outlined in the Appendix. The residual ΔI_m profiles are transformed to ΔB_ϕ for each orbit and shown in Figure 3.

The ΔB_ϕ profiles shown in Figure 3 still present a positive spatial gradient on B-ring connected field lines on the outbound leg of each orbit. The median ΔB_ϕ profile in Figure 3(b) goes to zero at the nominal r_C boundary, where the signal is negative planetward of this location and mostly zero outside, which is inconsistent with the Xin et al. (2006) picture of a diverging electric field at KSO. Although there is some orbit-by-orbit variability in the individual ΔB_ϕ profiles, the negative to

positive B_ϕ change seems to generally occur at r_C, or at the furthest, within the X06 boundary. In fact, the ΔB_ϕ profiles in Figures 3(a) and (b) are remarkably flat on L-shells between KSO and the outer edge of the B-ring, even though the polynomial was only fit to data that map to the L-shell beyond the outer edge of the B-ring (see the Appendix for more details). The largely constant B_ϕ and ΔB_ϕ outside of the KSO boundary suggest that the B-ring current may be localized to the region within the theoretical KSO boundary.

Looking at the data collectively, the spatial correlations between the H_3^+ emissions, the icy nanograin influx, and the field-aligned currents seem to suggest that the ring rain generation mechanism must be electromagnetically coupling Saturn and its rings. In fact, the ∼1.5–2.3 R_S constraints on the whistler mode wave emission source in the ring plane (see Figures 1 and 2) also do not exclude the possibility of multiple electron beam sources, or a spatially variable electron beam source, generated by ring rain dynamics. However, only the RPWS measurements, when observed in a stand-alone capacity, appear to be consistent with an emission source at the theoretical KSO boundary as predicted by the Xin current system.

3.3. Possible B-ring Current Generation Mechanism

The B-ring field-aligned currents presented in Figure 2 indicate a ringward current in both hemispheres, which is consistent with the net movement of planetward field-aligned electrons. Across the 21 Grand Finale orbits analyzed, the field-aligned currents are observed over an azimuthal extent of ∼1 local time hour in the southern hemisphere, over ∼5 months, with some orbit-by-orbit variability on week-long timescales. The presence of a persistent field-aligned current on such extended temporal and spatial scales implies that there must be a (semi)permanent electrically conducting layer near the rings that can facilitate current closure.

Seeing as the direction of the observed field-aligned current is consistent with the Xin generation mechanism but not the expected location of the ring plane mapping, we consider the ways in which the Xin current system can be altered. In principle, the generation mechanism behind the Xin current system is identical to the driver of the intra D-ring currents. Both field-aligned current systems are supported by an angular velocity shear in the azimuthal (east–west) motion of neutral particles in two different plasma layers connected by the same magnetic field line.

An adapted version of the Provan et al. (2019b) equation used to model the meridional current I_m associated with the intra D-ring current system is presented in Equation (2), where the subscripts have been modified from the original equation such that r and S now denote parameters associated with the ring ionosphere and Saturn's ionosphere, respectively:

$$I_m(\theta_i) = \frac{\Sigma_{\mathrm{Pr}}\Sigma_{PS}(\Omega_S - \Omega_r)}{\Sigma_{\mathrm{Pr}}[1/(\rho_{iS}^2 B_{iS})] + \Sigma_{PS}[1/(\rho_{ir}^2 B_{ir})]}. \quad (2)$$

Here, Ω is the angular velocity of the neutral particles, Σ_P is the Pedersen conductance of the ionosphere, B_i is the total magnetic field strength normal to the ionospheric layer, and ρ_i is the perpendicular distance between the ionospheric footprint of the magnetic field line and Saturn's dipole axis. The sense of the angular velocity shear as stated in Equation (2) applies only to the northern hemisphere and should be reversed, i.e., $(\Omega_r - \Omega_S)$, for calculations associated with the southern hemisphere.

Field-aligned currents are driven by spatial gradients in I_m. Therefore, Equation (2) shows that a large spatial gradient in either the angular velocity shear or Pedersen conductance at the footpoints of adjacent magnetic field lines would be required to generate the localized ∼0.8 nA m^{-2} field-aligned current at the ∼1.61 R_S L-shell that has been reported in this study.

The ∼1.55–1.67 R_S L-shell maps to the latitudinal range of ∼36°–39°S in Saturn's ionosphere, where neither the zonal winds (Brown et al. 2020) nor the Pedersen conductance (Agiwal et al. 2021) are expected to vary significantly over a ∼3° latitude range. Therefore, the spatial gradient must exist in the ring plane.

The Keplerian angular velocities of ring atmosphere neutrals are expected to decrease with radial distance from Saturn with the relationship $r^{-3/2}$, which would yield small incremental changes in the angular velocity on adjacent magnetic field lines between ∼1.5 and 1.7 R_S. The neutral ring velocities would have to be slowed down by ∼20% from their Keplerian orbit due to processes such as inter-ring collisions (Xin et al. 2006; Sulaiman et al. 2019) for a large spatial gradient in the angular neutral velocity to be observed in our region of interest. While we cannot disprove the idea, there is also no evidence to suggest that the ring particles would deviate so significantly from their Keplerian orbits.

Finally, a localized field-aligned current at this limit could be generated by a gradient in the Pedersen conductance in the ring ionosphere. There are no observational constraints on the Pedersen conductance of the ring ionosphere as yet. However, we have extensively discussed the modeled ∼1.55–1.67 R_S critical radius boundary that is associated with the ring rain generation mechanism in Saturn's upper atmosphere and is closely located with the sharp increase in optical depth between the inner and outer B-ring (Northrop & Hill 1983b). It is plausible that the ring rain generation mechanism, which separates the ring plasma into regions of atmospheric loss (within the critical radius) and equatorial confinement (outside the critical radius), might also divide the ring ionosphere into regions of relatively high and low Pedersen conductance.

On average, the field-aligned currents are only observed on L-shells inward of ∼1.65 R_S (see Figure 2(c)). If we assume that the field-aligned currents are generated by a gradient in Pedersen conductance of the ring ionosphere, the observations would imply that the gradient is the strongest at the ∼1.65 R_S boundary, with a higher ring ionosphere Pedersen conductance within the boundary and lower Pedersen conductance outside, since a return current is not consistently observed beyond ∼1.65 R_S. Meanwhile, the intra D-ring currents flow into Saturn's atmosphere in the southern hemisphere, radially inward of where the B-ring current is detected, which is consistent with the expected direction of the B-ring return current.

The average intra D-ring field-aligned current density is $\sim 3 \pm 1.08$ nA m^{-2} in the southern hemisphere and $\sim 2 \pm 1.14$ nA m^{-2} in the northern hemisphere between the ∼1.1 and 1.23 R_S L-shells. In the southern hemisphere, the B-ring $|j_{||}|$ is $\sim 0.8 \pm 0.4$ nA m^{-2}. The B-ring currents are notably weaker than the intra D-ring currents; thus, both signals remain observationally indistinguishable in the southern hemisphere, supporting the possibility of the B-ring current closing as part of the intra D-ring current loop.

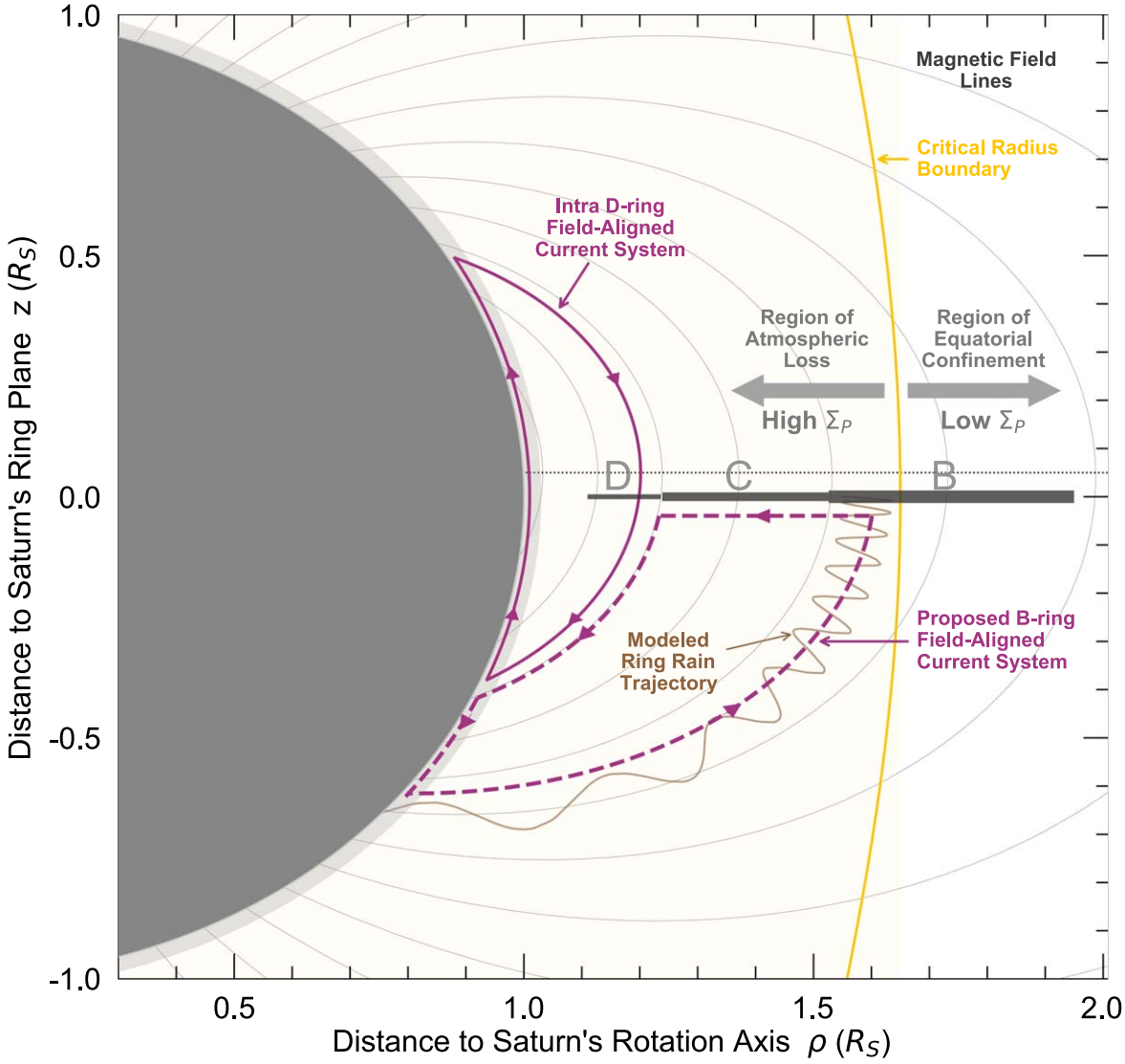

Figure 4. This figure follows the same general format as Figure 1. The interhemispheric, intra D-ring field-aligned current system is shown using solid pink lines. Meanwhile, the proposed flow and closure of the B-ring field-aligned current system is shown using dashed pink lines. Pink arrows indicate the direction of current flow for both current systems. Large gray arrows and corresponding labels indicate the bifurcation of ring plasma properties inferred from our analysis that would control the pathways of current closure.

Thus, we propose that the observed B-ring currents close by flowing radially toward Saturn in the ring plane until they reach the C/D-ring boundary. This boundary is characterized by a sharp decrease in the optical depth and density from the C-ring to the D-ring, which would prohibit further radial current flow. Consequently, the B-ring currents are redirected to flow into Saturn's ionosphere along the magnetic field at a similar *L*-shell to the intra D-ring currents. In Saturn's ionosphere, the two current systems diverge meridionally, and the southward ($+z$ direction) component closes the B-ring current loop. An illustration of the proposed current system associated with the B-ring signature is shown in Figure 4.

Our proposed pathway of current closure is also consistent with currents generated by the $\boldsymbol{v} \times \boldsymbol{B}$ electric field proposed by Xin et al. (2006). The addition of the ring rain generation mechanism controls the permissible pathways that the Xin currents can take by altering the Pedersen conductance of the ring ionosphere on either side of the critical radius boundary. Alternate pathways for current closure may also be plausible, i.e., if the B-ring currents were to flow azimuthally in the ring plane and close at a different local time in the magnetosphere. However, there are insufficient observations to explore this option without significant additional modeling effort, which is beyond the scope of this study. The current system illustrated in Figure 4 offers the simplest pathway for the B-ring currents to close in Saturn's magnetosphere.

Using Equation (2) and the field-aligned current density observed in the southern hemisphere, we can constrain the Pedersen conductance of the ring ionosphere inside $\sim$1.65 R_S. Based on simulations by Tseng et al. (2010), the vertical extent of the ring ionosphere is assumed to be $<$0.1 R_S above and below the ring plane within $\sim$1.65 R_S, with north–south asymmetries due to the magnetic equator offset and seasonal conditions. Due to a lack of in situ measurements in this region, using the magnetic field measurements and Equation (2) is also the only way to empirically constrain the Pedersen conductance of the ring ionosphere.

We employ a degree-3 internal field model (Dougherty et al. 2018; Cao et al. 2020) to evaluate the magnetic field components in Saturn's ionosphere and the ring plane. Saturn's

neutral upper atmosphere is assumed to be perfectly corotating with the planet, and the neutral ring particles are assumed to be orbiting at Keplerian velocities in the ring plane. The Pedersen conductance of Saturn's midlatitude southern hemisphere ionosphere is taken as $\Sigma_P \sim 1$ S from the STIM-GCM model (Müller-Wodarg et al. 2019; Agiwal et al. 2021).

Since $j_{||}/B$ must be conserved along the magnetic field, we scale the observed $j_{||}$ by a factor of $\frac{B_i}{B_{sc}}$, which gives the ratio of the magnetic field strength in the ionosphere (B_i) and at the spacecraft position (B_{sc}). We use the median value of $j_{||} \sim 0.8$ nA m^{-2} in the southern hemisphere to constrain the typical Pedersen conductance of the high-conductance ring ionosphere region, which we propose lies radially inward of $\sim$1.65 R_S. The associated $j_{||}$ above the ionosphere is estimated to be $\sim$1.9 nA m^{-2}, which, integrated over $\sim$1 rad in azimuth and $\sim$3° in latitude, gives a total meridional current of $\sim$0.2 MA per azimuth radian. Rearranging Equation (2) for Σ_{Pr}, we evaluate the average ring ionosphere Pedersen conductance in the high-conductance ring ionosphere region to be $\sim$0.1 S, which is an order of magnitude smaller than the conductance in Saturn's ionosphere.

The orbit-by-orbit variability in the amplitude and L-shell mapping of the southern hemisphere signal also implies that the ring ionosphere is a temporally variable structure. Therefore, we use the smallest and largest $j_{||}$ values presented in Figure 2 of $\sim$0.4 nA m^{-2} and 1.2 nA m^{-2}, respectively, to constrain the variability of ring ionosphere Pedersen conductance to 0.07–2 S on week-long timescales. For a ring ionosphere with a maximum vertical extent of $\sim$0.1 R_S in any one hemisphere ($\sim$6000 km; Tseng et al. 2010), this corresponds to Pedersen conductivities on the order of $\sim 10^{-7}$–10^{-8} S m^{-1}, which are indeed very small and thus consistent with a tenuous ring ionosphere and the very weak currents ($\sim$1 nA m^{-2}) that were detected during the Grand Finale orbits.

The ion photoproduction rate is often assumed to be the dominant ring atmosphere ionization source (e.g., Luhmann et al. 2006; Tseng et al. 2010); however, it is not expected to vary significantly on week-long timescales. Thus, we might anticipate a secondary, more variable ionization source that could alter the ring ionosphere on week-long timescales. Ip (1984) and Northrop & Connerney (1987) have suggested that ions with variable plasma properties may be generated by random meteoroid impacts, which is consistent with the northward ring rain signatures observed by O'Donoghue et al. (2013) and Hsu et al. (2018) and could subsequently alter the ring ionosphere densities and Pedersen conductance.

4. Conclusions

This study delivers a comprehensive analysis that combines in situ and ground-based observations, aiming to unravel the electromagnetic connection between Saturn's rings and its atmosphere. Our primary motivation was to understand the Cassini MAG's detection of field-aligned currents linked to Saturn's B-ring during the Grand Finale orbits.

The key results from our study are as follows.

1. The field-aligned currents observed on B-ring connected magnetic field lines present a significant north–south hemispheric asymmetry in amplitude, occurrence frequency, and L-shell mapping. This asymmetry strongly suggests that, in contrast to the intra D-ring currents, the B-ring currents are generated by electromagnetic coupling between Saturn's upper atmosphere and an external plasma source, i.e., the rings.
2. All four data sets considered in this study (ground-based H_3^+ emissions in Saturn's atmosphere, Cassini CDA detection of nanograin influx at low-to-midlatitudes, Cassini RPWS signatures of whistler mode waves emitted from Saturn's main rings, and the B-ring MAG signal) feature a north–south hemispheric asymmetry, where the signal is typically stronger and observed more frequently in the southern hemisphere.
3. The stronger CDA and H_3^+ emission signals in the southern hemisphere suggest that the near-ring plasma environment preferentially leads to negative dust grain potential.
4. The MAG measurements do not show any evidence of persistent field-aligned currents near the Kronosynchronous orbital radius suggested by Xin et al. (2006).
5. Our proposed mechanism for the field-aligned current generation involves a superposition of the Xin current system and ring rain. The field-aligned currents are generated by a $\boldsymbol{v} \times \boldsymbol{B}$ electric field, as predicted by Xin et al. (2006). However, the regulation of current flow occurs through the ring rain generation mechanism, which dictates the permissible pathways for these currents by controlling the ring ionosphere Pedersen conductance.
6. Although field-aligned currents were not an expected signature of the ring rain generation mechanism, we show that they are an unanticipated manifestation of the process that separates the ring ionosphere into regions of relatively high and low Pedersen conductance. The Pedersen conductance of the high-conductance region (i.e., inward of $\sim$1.65 R_S) is evaluated to be $\sim$1 S, on average; however, observations show that this parameter is likely variable between 0.07 and 2 S on week-long timescales.

Additionally, some outstanding questions remain.

1. Although we suggest a pathway for the B-ring currents to close, there is insufficient evidence to prove whether this is the sole pathway for current closure.
2. If the generation of the field-aligned currents is primarily controlled by the Pedersen conductance of the ring ionosphere, then why are the northern hemisphere currents (the sunlit side) so much weaker? Tseng et al. (2010) show that the ring ionosphere is typically denser in the southern hemisphere, irrespective of season; however, we would need more observations or modeling work to investigate the effect of this density gradient on the ring ionosphere's ability to conduct currents.
3. Could a magnetic signature of ring rain be expected at other giant planets with rings? Or is the magnetic signature unique to Saturn, given the surface density of its rings?

Acknowledgments

O.A. and L.M. acknowledge support by NASA grant No. 80NSSC21K0157 issued through the Solar System Workings Program. H.C. acknowledges support by the NASA Cassini Data Analysis Program (grant No. 80NSSC23K0511). H.-W.H. acknowledges the support from the NASA ROSES CDAP

grant No. 80NSSC24K0423. A.H.S. acknowledges NASA grant No. 80NSSC23K0334. J.O. is supported by the Science and Technologies Facilities Council's Ernest Rutherford Fellowship grant No. ST/X003426/1. M.K.D. is funded by Royal Society, UK Research Professorship RP140004. This research was also supported by the "New View of Ring-Planet Interactions From Cassini's Grand Finale" team meeting, hosted by the International Space Science Institute.

Cassini magnetometer data supporting this work are publicly available on the Imperial College London MAGDA server (https://magda.imperial.ac.uk/) and the NASA Planetary Data System at the Jet Propulsion Laboratory (https://pds.jpl.nasa.gov/).

Appendix
External Perturbation Field Subtraction from Ring-connected Grand Finale MAG Data

PPOs typically manifests as a ∼10.6 hr sinusoidal perturbation in observations. The PPO perturbation field rotates through Saturn's magnetosphere with a ∼10.6 hr period and thus varies with azimuthal position in the magnetosphere as well. Based on the spacecraft trajectory, Cassini traversed ∼4.5 hr of the PPO perturbation field during each Grand Finale orbit (Provan et al. 2019b; Agiwal et al. 2021), which is just under half of one full PPO perturbation. Therefore, we perform the subtraction as follows.

1. We transform the B_ϕ measurements to I_m using Equation (1), since we want to subtract the effect of an additional current system from the measurement that also scales with distance from the planet.
2. The B_ϕ and I_m data are remarkably flat on magnetic field lines connected to L-shells $>1.95\,R_S$ (B-ring outer edge) for both the inbound and outbound segments of each orbit (see Figure 2). Therefore, we assume that the lack of gradients signifies a constant external current system, such as the PPOs.
3. For each orbit, subtract an $n = 2$ polynomial (same profile as approximately half of a sinusoidal perturbation) from the data by fitting the polynomial simultaneously to the inbound and outbound I_m for L-shells between 1.95 and $2.26\,R_S$ (B-ring outer edge to A-ring outer edge, respectively). The data intervals that are used for the polynomial fitting are highlighted by red arrows in Figure 3.
4. The polynomial subtracted I_m profiles are transformed back to B_ϕ using Equation (1) and presented in Figure 3.

ORCID iDs

Omakshi Agiwal https://orcid.org/0000-0003-3999-9926
Hao Cao https://orcid.org/0000-0002-6917-8363
Hsiang-Wen Hsu https://orcid.org/0000-0002-5478-4168
Luke Moore https://orcid.org/0000-0003-4481-9862
Ali H. Sulaiman https://orcid.org/0000-0002-0971-5016
James O'Donoghue https://orcid.org/0000-0002-4218-1191
Michele K. Dougherty https://orcid.org/0000-0002-9658-8085

References

Agiwal, O. 2024, Cassini Magnetometer Data Products Associated With Ring-Saturn Electromagnetic Coupling, Zenodo, doi:10.5281/ZENODO.10823289
Agiwal, O., Cao, H., Cowley, S. W. H., et al. 2021, JGRE, 126, e06578
Andrews, D. J., Bunce, E. J., Cowley, S. W. H., et al. 2008, JGRA, 113, A09205
Bouhram, M., Johnson, R. E., Berthelier, J. J., et al. 2006, GeoRL, 33, 5106
Brown, Z., Koskinen, T., Müller-Wodarg, I., et al. 2020, NatAs, 4, 872
Buchert, S. C. 2020, AnGeo, 38, 1019
Cao, H., Dougherty, M. K., Hunt, G. J., et al. 2020, Icar, 344, 113541
Carbary, J. F., & Mitchell, D. G. 2013, RvGeo, 51, 1
Connerney, J. E. P. 1986, GeoRL, 13, 773
Connerney, J. E. P. 2013, Natur, 496, 178
Dougherty, M. K., Cao, H., Khurana, K. K., et al. 2018, Sci, 362, eaat5434
Dougherty, M. K., Kellock, S., Southwood, D. J., et al. 2004, SSRv, 114, 331
Farrell, W. M., Hadid, L. Z., Morooka, M. W., et al. 2018, GeoRL, 45, 8104
Gurnett, D. A., Kurth, W. S., Kirchner, D. L., et al. 2004, SSRv, 114, 395
Hadid, L. Z., Morooka, M. W., Wahlund, J.-E., et al. 2018, GeoRL, 46, 9362
Hsu, H. W., Schmidt, J., Kempf, S., et al. 2018, Sci, 362, eaat3185
Hunt, G. J., Cowley, S. W., Provan, G., et al. 2014, JGRA, 119, 9847
Hunt, G. J., Cowley, S. W. H., Provan, G., et al. 2019, JGRA, 124, 5675
Ip, W.-H. 1983, JGR, 88, 819
Ip, W. H. 1984, JGR, 89, 395
Ip, W. H., Liu, C. M., & Pan, K. C. 2016, Icar, 276, 163
Johnson, R., Luhmann, J., Tokar, R., et al. 2006, Icar, 180, 393
Khurana, K. K., Dougherty, M. K., Provan, G., et al. 2018, GeoRL, 45, 10,068
Luhmann, J., Johnson, R., Tokar, R., Ledvina, S., & Cravens, T. 2006, Icar, 181, 465
Moore, L., O'Donoghue, J., Müller-Wodarg, I., Galand, M., & Mendillo, M. 2015, Icar, 245, 355
Müller-Wodarg, I. C. F., Koskinen, T. T., Moore, L., et al. 2019, GeoRL, 46, 2372
Northrop, T. G., & Connerney, J. E. P. 1987, Icar, 70, 124
Northrop, T. G., & Hill, J. R. 1982, JGR, 87, 6045
Northrop, T. G., & Hill, J. R. 1983a, JGR, 88, 819
Northrop, T. G., & Hill, J. R. 1983b, JGR, 88, 6102
O'Donoghue, J., Moore, L., Connerney, J., et al. 2019, Icar, 322, 251
O'Donoghue, J., Moore, L., Connerney, J. E. P., et al. 2017, GeoRL, 44, 11,762
O'Donoghue, J., Stallard, T. S., Melin, H., et al. 2013, Natur, 496, 193
Persoon, A. M., Kurth, W. S., Gurnett, D. A., et al. 2020, JGRA, 125, e27545
Provan, G., Cowley, S. W. H., Bunce, E. J., et al. 2019a, JGRA, 124, 379
Provan, G., Cowley, S. W. H., Bunce, E. J., et al. 2019b, JGRA, 124, 8814
Provan, G., Lamy, L., Cowley, S. W. H., & Bunce, E. J. 2019c, JGRA, 124, 1157
Srama, R., Ahrens, T. J., Altobelli, N., et al. 2004, SSRv, 114, 465
Sulaiman, A. H., Farrell, W. M., Ye, S., et al. 2019, GeoRL, 46, 7166
Sulaiman, A. H., Kurth, W. S., Hospodarsky, G. B., et al. 2018a, GeoRL, 45, 7347
Sulaiman, A. H., Kurth, W. S., Hospodarsky, G. B., et al. 2018b, GeoRL, 45, 6782
Tseng, W. L., Ip, W. H., Johnson, R. E., Cassidy, T. A., & Elrod, M. K. 2010, Icar, 206, 382
Tseng, W. L., Johnson, R. E., & Elrod, M. K. 2013, P&SS, 77, 126
Wahlund, J. E., Morooka, M. W., Hadid, L. Z., et al. 2018, Sci, 359, 66
Xin, L., Gurnett, D. A., Santolík, O., Kurth, W. S., & Hospodarsky, G. B. 2006, JGRA, 111, A06214